Max-Planck-Institut
für Meteorologie

REPORT No. 26

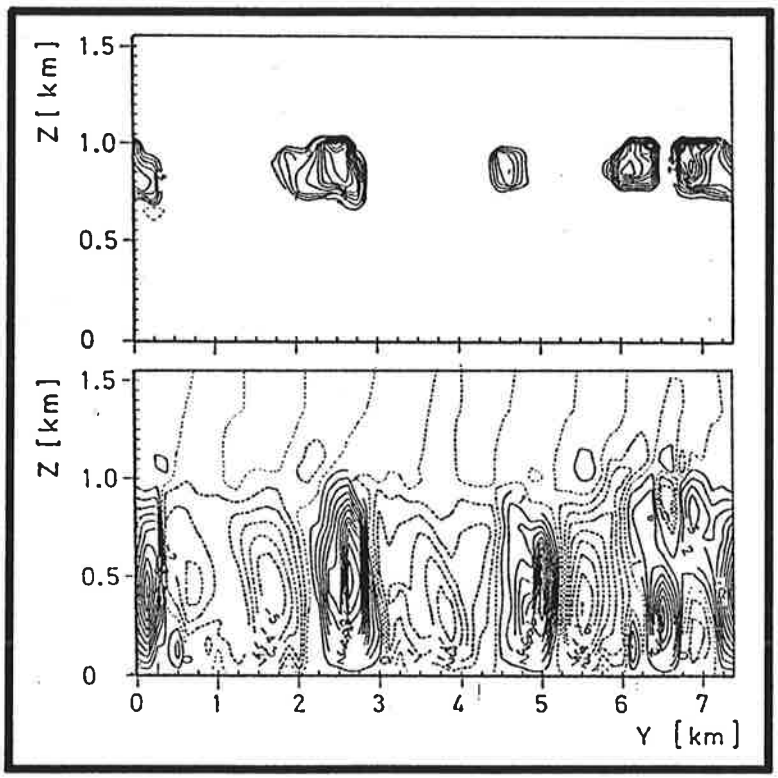

NUMERICAL INVESTIGATION OF ORGANIZED CUMULUS CONVECTION: A CASE STUDY

by

PAUL BECKER

HAMBURG, APRIL 1989

AUTHOR:

PAUL BECKER

METEOROLOGISCHES INSTITUT
DER UNIVERSITAET HAMBURG
BUNDESSTRASSE 55
2000 HAMBURG 13
F. R. GERMANY

MAX-PLANCK-INSTITUT
FUER METEOROLOGIE
BUNDESSTRASSE 55
D-2000 HAMBURG 13
F.R. GERMANY

Tel.: (040) 4 11 73-0
Telex: 211092
Telemail: MPI.Meteorology
Telefax: (040) 4 11 73-298

Numerical Investigation of Organized Cumulus Convection: A Case Study

Paul Becker
Meteorologisches Institut der Universität Hamburg
Bundesstraße 55, 2000 Hamburg 13, FRG

Contents

1 Abstract

The influence of small non-precipitating cumulus clouds on buoyancy generated horizontal roll vortices is investigated by means of a two-dimensional numerical grid point model. The length of the model domain is 7.375 km in the horizontal direction and 2.05 km in the vertical direction with a grid spacing of 125 m horizontally and 50 m vertically. The large-scale two-dimensional eddies are calculated explicitly by the model, while the small-scale turbulence is parameterized by a buoyancy and wind-shear dependent mixing-length approach.
The model is applied to conditions corresponding to an observed case of cloud street development (which occurred over the North Sea during the 1981 KonTur experiment). Results are described for two simulations. The first run simulates a case of roll activity neglecting phase change effects, while in the second run the condensation process is incorporated. In this manner the importance of the influence of the clouds on the secondary circulation and the roll-scale transports can be ascertained. Qualitative and quantitative descriptions of the flow field for the moist and the dry case are given. Additionally, the roll-scale velocity variances and the vertical transports of temperature, humidity and along- and cross-roll momentum are compared with observations.

2 Introduction

Horizontal roll vortices often visualized by cloud streets forming over the upward mooving branches, are a frequent phenomenon in the atmospheric boundary layer. Observations (e.g. KUETTNER, 1971 and LE MONE, 1973) yielded some of the characteristic roll scales. The length of the parallel arranged cloud bands range from 20 to 500 km and the horizontal wavelength shows variations between 2 and 8 km. The vertical extension of the vortices ranges from 0.8 km to 3 km and the aspect ratios show values between 2 and 4. Since these organized convective motions transport and redistribute momentum and energy it seems reasonable to suppose that there are important feedback effects between the convective motions and the large-scale mean flow. Consequently, the formation of the longitudinal vortex rolls in fluid layers has been subjected to numerous experimental and numerical studies.
BROWN (1970) and WIPPERMANN et al. (1978) developed linear models to investigate the instability mechanismen. These models gave already the scales and orientations of the rolls. Additionally two- and three-dimensional nonlinear models were developed in order to simulate the development of the rolls in neutrally and unstably stratified atmospheric boundary layers (MASON and SYKES, 1980, 1982, CHLOND, 1987, BECKER, 1987). However, the influence of the condensation process was neglected in most studies on this topic. In order to investigate also the influence of the clouds on the secondary circulation and the transports this limitation has been alleviated in the present study (by allowing small non-precipitating clouds). The rolls are assumed to be two-dimensional and are modelled explicitly in a vertical plane of fixed orientation with respect to the geostrophic wind. Although the model is far from being perfect for the simulation of such complex boundary layer phenomena, it can give at least some insight in the exchange processes between the roll circulation and the clouds. The model is similar to those developed by MASON (1985) and SYKES, LEWELLEN and HENN (1988). But in contrast to these investigators we do not use the concept of the liquid water potential temperature. In the present study the full set of primitive equations (momentum, heat, specific humidity and specific liquid water content) is solved.
In section 3 the numerical techniques and the boundary conditions are outlined. In section 4 the model is applied to conditions corresponding to an observed case of cloud street development (which occurred over the North Sea during the KonTur experiment). Results are described for two simulations. The two simulations begin with an identical initialization, but differ in that way that one run includes the condensation process whereas the other run does not. Qualitative and quantitative descriptions of the secondary circulations for the dry and the moist case are given. Additionally, the calculated roll-scale velocity variances and the vertical transports of along- and cross-roll momentum, of heat and of humidity are compared with measurements. Finally we will discuss and summarize our results.

3 The Numerical Model and Governing Equations

3.1 Governing Equations

The fluid is supposed to consist of a mixture of two perfect gases, air and water vapour, containing water droplets in suspension. The basic variables include the u, v and w component of the velocity, the potential temperature (θ), the specific humidity (q), the specific liquid water content (q_l) and the perturbation pressure. In some instances (e.g. the buoyancy term in the vertical velocity equation) two other thermodynamic variables are used, the virtual potential temperature $\theta_v = (1. + 0.61q)\theta$ and $\theta_{vl} = (1 + 0.61q - q_l)\theta$ (a potential temperature taking into account the weight of liquid water). The used equations are the Reynolds-averaged equations for a Boussinesq fluid written in Cartesian (x, y, z) co-ordinates. Molecular terms are neglected due to the high Reynolds numbers occuring in this kind of studies. Additionally, the horizontal component of the Coriolis parameter is neglected. The equations then read:

$$\frac{\partial u}{\partial x} + \frac{\partial v}{\partial y} + \frac{\partial w}{\partial z} = 0, \tag{1}$$

$$\frac{\partial u}{\partial t} = -\frac{1}{\rho_0}\frac{\partial p^*}{\partial x} - \frac{1}{\rho_0}\frac{\partial p_S}{\partial x} + fv - u\frac{\partial u}{\partial x} - v\frac{\partial u}{\partial y} - w\frac{\partial u}{\partial z} + \frac{\partial \tau_{xx}}{\partial x} + \frac{\partial \tau_{xy}}{\partial y} + \frac{\partial \tau_{xz}}{\partial z} + (\frac{\partial u}{\partial t})_{L.SC.}, \tag{2}$$

$$\frac{\partial v}{\partial t} = -\frac{1}{\rho_0}\frac{\partial p^*}{\partial y} - \frac{1}{\rho_0}\frac{\partial p_S}{\partial y} - fu - u\frac{\partial v}{\partial x} - v\frac{\partial v}{\partial y} - w\frac{\partial v}{\partial z} + \frac{\partial \tau_{yx}}{\partial x} + \frac{\partial \tau_{yy}}{\partial y} + \frac{\partial \tau_{yz}}{\partial z} + (\frac{\partial v}{\partial t})_{L.SC.}, \tag{3}$$

$$\frac{\partial w}{\partial t} = \frac{g}{\theta_0}\theta_{vl} - u\frac{\partial w}{\partial x} - v\frac{\partial w}{\partial y} - w\frac{\partial w}{\partial z} + \frac{\partial \tau_{zx}}{\partial x} + \frac{\partial \tau_{zy}}{\partial y} + \frac{\partial \tau_{zz}}{\partial z} + (\frac{\partial w}{\partial t})_{L.SC.}, \tag{4}$$

$$\frac{\partial \theta}{\partial t} = -u\frac{\partial \theta}{\partial x} - v\frac{\partial \theta}{\partial y} - w\frac{\partial \theta}{\partial z} + \frac{\partial \tau_{\theta x}}{\partial x} + \frac{\partial \tau_{\theta y}}{\partial y} + \frac{\partial \tau_{\theta z}}{\partial z} + (\frac{\partial \theta}{\partial t})_C + (\frac{\partial \theta}{\partial t})_{L.SC.}, \tag{5}$$

$$\frac{\partial q}{\partial t} = -u\frac{\partial q}{\partial x} - v\frac{\partial q}{\partial y} - w\frac{\partial q}{\partial z} + \frac{\partial \tau_{qx}}{\partial x} + \frac{\partial \tau_{qy}}{\partial y} + \frac{\partial \tau_{qz}}{\partial z} + (\frac{\partial q}{\partial t})_C + (\frac{\partial q}{\partial t})_{L.SC.}, \tag{6}$$

$$\frac{\partial q_l}{\partial t} = -u\frac{\partial q_l}{\partial x} - v\frac{\partial q_l}{\partial y} - w\frac{\partial q_l}{\partial z} + \frac{\partial \tau_{q_l x}}{\partial x} + \frac{\partial \tau_{q_l y}}{\partial y} + \frac{\partial \tau_{q_l z}}{\partial z} - (\frac{\partial q}{\partial t})_C + (\frac{\partial q_l}{\partial t})_{L.SC.}. \tag{7}$$

p^* is the perturbation pressure, ρ is the density and g is the acceleration due to gravity. c_P is the specific heat coefficient at constant pressure, f is the Coriolis parameter, $\tau_{i,j}$ are the subgrid scale Reynolds stresses or the subgrid scale temperature and humidity fluxes. The determination of the turbulent terms is the object of section 3.2. The C and $L.SC.$ indizes refer respectively to the effects of condensation and large scale advection. The possibility of considering large-scale effects is useful because it gives more flexibility to the model in order to treat actual meteorological cases and allows the existence of quasi long-term steady states with balanced budgets of momentum, heat and water. The subscript "S" denotes the synoptic state and the subscript "0" denotes a reference state. The reference density ρ_0 is chosen to be independent of height. This approximation is justified for shallow convection (DUTTON and FICHTEL, 1969). $\partial p_S/\partial x$ and $\partial p_S/\partial y$ (the horizontal pressure gradients) are assumed to be constant in space and time and are related to the geostrophic wind vector by:

$$\frac{1}{\rho_0 f}\frac{\partial p_S}{\partial x} = v_g, \qquad -\frac{1}{\rho_0 f}\frac{\partial p_S}{\partial y} = u_g. \tag{8}$$

The perturbation pressure field is obtained by taking the divergence of the equation of motions and forming a Poisson equation:

$$\frac{\partial \psi_1}{\partial x} + \frac{\partial \psi_2}{\partial y} + \frac{\partial \psi_3}{\partial z} = \nabla^2 p^*, \tag{9}$$

ψ_1, ψ_2 and ψ_3 are the sums of the right-hand sides (except the p^* gradient terms) of the equations (2), (3) and (4). With equation (9) it is possible to determine the pressure perturbation field as a function of the velocity and temperature field. The Poisson equation from which the perturbation pressure p^* is obtained was solved by employing the successive overrelaxation method (SOR).
Although observations and numerical experiments indicate that there are three-dimensional elements in the quasi-two-dimensional structures we only use a two-dimensional model due to the limitations of computer resources. We choose a coordinate system, where the $x-$axis points in the direction of the vortex roll axis. The roll vortices are hence obtained as two-dimensional solutions in the y-$z-$plane, assuming horizontal homogenity in the $x-$direction.

3.2 Subgrid Parameterization

Representation of the subgrid-scale turbulent fluxes is in this study accomplished through first order closure i.e., it is assumed that the subgrid-scale stresses are proportional to the gradients of the corresponding quantities:

$$\tau_{ij} = k_m(\frac{\partial u_i}{\partial x_j} + \frac{\partial u_j}{\partial x_i}). \tag{10}$$

k_m is the vertical diffusion coefficient for momentum. Heat and humidity fluxes are also proportional to the gradients of the corresponding quantities through a k_θ and a k_q coefficient:

$$\tau_{\theta,i} = k_\theta \frac{\partial \theta}{\partial x_i}, \qquad \tau_{q,i} = k_q \frac{\partial q}{\partial x_i}. \tag{11}$$

No distinction has been made here between water vapour and liquid water which are supposed to present the same turbulent characteristics.
The eddy viscosity is parameterized by a mixing length approach, similar to that used by MASON and SYKES (1982). In this formulation the local values of the eddy viscosity k_m are a function of the local wind shear, stability and height, according to the following relationship:

$$k_m = (\frac{l}{\phi})^2 S, \tag{12}$$

where S is the determinante of the deformation tensor of the velocity field.

$$S = \sqrt{\frac{1}{2}(\frac{\partial u_i}{\partial x_j} + \frac{\partial u_j}{\partial x_i}) \cdot (\frac{\partial u_i}{\partial x_j} + \frac{\partial u_j}{\partial x_i})}. \tag{13}$$

Thermal stratification is included via the Dyer-Businger similarity functions, which are related to a local Richardson number by:

$$Ri = \frac{g}{\theta_0} \frac{\partial \theta_v / \partial z}{(\partial u_i/\partial x_k + \partial u_j/\partial x_i)\partial u_i/\partial x_k} \tag{14}$$

The mixing length l is taken from BLACKADAR (1962):

$$l = \frac{\kappa z}{1 + \frac{z\kappa}{\lambda}} \tag{15}$$

κ is the von Kármán constant and λ is the asymptotic mixing length. ϕ is given by:

$$\phi = \begin{cases} 1 + 6Ri & Ri \geq 0 \\ (1 - 15Ri)^{-0.25} & Ri < 0 \end{cases} \tag{16}$$

The eddy diffusivity of heat (k_θ), specific humidity (k_q) and liquid water content (k_{q_l}) were related to k_m simply by $k_{(\theta,q,q_l)} = 1.35\, k_m$. For stability purposes, in the momentum equations only, a small background value of k_m ($2\ m^2/s$) was added. A background mixing in the equation of heat would lead to an unrealistic reduction of the inversion strength.

3.3 Condensation Cycle

In order to take into account the condensation process the model predicts the specific humidity and the specific liquid water content. The formulation is similiar to that used by SOMMERIA (1976). Therefore only a brief outline will be given here. Condensation occurs in this concept as soon as saturation is reached at a given grid point. If a grid volume is found to be saturated, it is assumed to be uniformly saturated throughout the whole grid volume. Supersaturation and precipitation are disregarded which is justified insofar as we are only interested in shallow convection. The saturation specific humidity is computed from:

$$q_s = \frac{\epsilon e_s}{p - (1 - \epsilon) e_s}, \tag{17}$$

where ϵ is the ratio of molecular masses for water vapour and air ($\epsilon = 0.622$). e_s is the saturation water vapour pressure.

$$e_s = 6.11 \cdot 10^{-2} exp[\frac{17.269(T - 273.16)}{T - 35.86}] \tag{18}$$

The source terms due to condensation are computed through a one step saturation adjustment.

$$\delta q_l = -q_l, \ if \ q < q_s \ and \ q_l < \frac{c_p R T^2}{\epsilon q_s L_v^2 + c_p R T^2}(q_s - q), \tag{19}$$

$$\delta q_l = \frac{c_p R T^2}{\epsilon q_s L_v^2 + c_p R T^2}(q - q_s), \ in \ other \ cases$$

$$\delta q = -\delta q_l \tag{20}$$

$$\delta\theta = (\frac{p_0}{p})^{(\gamma-1)/\gamma}\frac{L_v}{c_p}\delta q_l. \tag{21}$$

γ is the ratio of the specific heat coefficient at constant pressure and constant volume. L_v is the specific latent heat for vaporization.

3.4 Boundary Conditions

For the simulation described in subsequent section the following boundary conditions are used. At the lower boundary Monin-Obukhov similarity between the sea-surface and the first computational grid point is used in order to resolve the strong vertical gradients in the surface layer. Therefore we have:

$$u(z) = \frac{1}{\kappa} u_* cos\alpha [ln(z/z_0) - \Psi_M(z/L)], \tag{22}$$

$$v(z) = \frac{1}{\kappa} u_* sin\alpha [ln(z/z_0) - \Psi_M(z/L)],$$

$$\theta(z) = \theta(z_0) + \frac{\theta_*}{\kappa} [ln(z/z_0) - \Psi_H(z/L)].$$

A relation similar to that for the potential temperature is assumed to hold for the specific humidity as well. κ is the von Kármán constant and z_0 is the roughness length. L is the Monin-Obukhov scale height. The angle α is given by:

$$\alpha = arctan[\frac{v(z_P)}{u(z_P)}]. \tag{23}$$

The "friction" velocity u_* and the temperature scale θ_* are given as:

$$u_* = \frac{\kappa[u^2(z_P) + v^2(z_P)]^{1/2}}{ln(z_P/z_0) - \Psi_M(z_P/L)}, \qquad \theta_* = \frac{\kappa[\theta(z_P) - \theta(z_0)]}{ln(z_P/z_0) - \Psi_H(z_P/L)}, \tag{24}$$

where z_P is the height of the surface layer. Ψ_M and Ψ_H are functions of the stability parameter z/L and linked to the universal stability functions for momentum Φ_M and for heat Φ_H:

$$\Psi_M(z/L) = \int_{z_0}^{z_P} \frac{1 - \Phi_M(z/L)}{z} dz, \qquad \Psi_H(z/L) = \int_{z_0}^{z_P} \frac{1 - \Phi_H(z/L)}{z} dz. \tag{25}$$

Following BUSINGER et al. (1971) the universal stability functions $\Phi_H(z/L)$ and $\Phi_M(z/L)$ are given as:

$$\Phi_M(z/L) = (1 - 16z/L)^{-1/4}, \qquad \Phi_H(z/L) = 0.74(1 - 9z/L)^{-1/2}, \tag{26}$$

The Monin-Obukhov scale height is defined by:

$$L = \frac{u_*^2}{\kappa(g/\theta_0)\theta_*}. \tag{27}$$

The potential temperature at the sea surface was set equal to the sea temperature and was fixed in the numerical experiments. q_0 is chosen to be the saturation value at the sea surface.
At the upper boundary the vertical derivatives of the variables are supposed to remain equal to their initial values. The vertical velocity is set equal to its large scale value.

$$\frac{\partial u}{\partial z} = \frac{\partial v}{\partial z} = 0, \quad w = const, \quad \frac{\partial \theta}{\partial z} = const, \quad \frac{\partial q}{\partial z} = const \quad and \quad \frac{\partial q_l}{\partial z} = 0. \tag{28}$$

The upper boundary conditions do not allow transmissions of gravity waves which can be generated in the stable layer. This could lead to reflections and to an unrealistic distribution of momentum and energy. To avoid these unrealistic reflections a so called "Rayleigh-damping" is introduced in the stable layer of the model domain. The "Rayleigh-damping" is (due to the small vertical extension of the model (2.05 km)) used in the whole stable layer. Of course, this procedure affects the generation of gravity waves. It would be more favourable to use a deeper model domain. In such a model the "Rayleigh-damping" is only necessary in the uppermost part of the stably stratified layer. In this case the internal gravity waves can propagate away from the convective layer and be dissipated at higher levels without risk of reflection. But due to the limitations of the computer resources this was not done in the present work.
At the vertical sides cyclic boundary conditions are prescribed for the variables.

3.5 Numerical Scheme

3.5.1 The Grid

The staggered grid described by DEARDORFF (1973) was used for the simulations described below. With the use of such a grid the derivative in a non-linear advective term may be represented essentially by a difference across a single grid intervall, rather than across two intervalls as in the non-staggered mesh system. The temperature, the specific humitity and the specific liquid water content were located

at the same points as the vertical velocity owing to be the importance of the buoyancy term. Fig. 1 shows the grid.

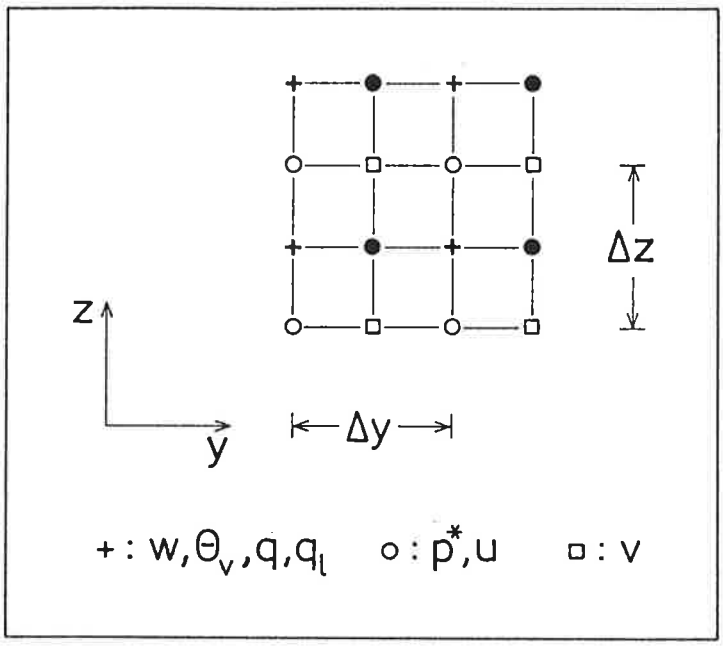

Fig. 1: Relative locations of pressure (p^*), the velocity components (u, v, w), virtual potential temperature (θ_v), specific humidity (q) and specific liquid water content (q_l) for the space staggered grid.

The model contains $60 * 42$ grid points in the used version. The horizontal grid increment is $125\,m$ and the vertical is $50\,m$. Therefore the physical domain has a length of $7.375\,km$ and a height of $2.05\,km$.

3.5.2 Nonlinear Advection Terms

The non linear advection terms are written in flux form because this formulation tends to conserve the spatially integrated kinetic energy. The recommended scheme is visualized by showing a typical term such as $\frac{\partial}{\partial z}(v\,w)$:

$$\frac{\partial}{\partial z}(v\,w) = \{\frac{1}{2}[v(j,k) + v(j,k+1)] * \frac{1}{2}[w(j,k+1) + w(j-1,k+1)] \qquad (29)$$

$$-\frac{1}{2}[v(j,k-1) + v(j,k)] * \frac{1}{2}[w(j,k) + w(j-1,k)]\}/\Delta z$$

3.5.3 Time differencing

The prognostic equations are solved by using the Adams-Bashforth scheme with a time step of 3 s.

$$f_i^{n+1} = f_i^n + \Delta t(\frac{3}{2}Q_i^n - \frac{1}{2}Q_i^{(n-1)}), \qquad (30)$$

where $Q_i = \partial u_i/\partial t$. n is the time index and Δt the time step.

3.5.4 Correction of the Poisson Equation

To ensure incompressibility, the Poisson equation is solved by applying the numerical divergence operator $\delta/\delta x_i$ to the numerical form of the equation of motion. The Poisson equation can be written as:

$$\frac{\partial}{\partial t}(\frac{\partial v}{\partial y} + \frac{\partial w}{\partial z}) = \frac{\partial \psi_2}{\partial y} + \frac{\partial \psi_3}{\partial z} - \frac{1}{\rho_0}\nabla^2 p^*, \qquad (31)$$

The left hand side of (31) can be expressed as:

$$[(\frac{\partial v}{\partial y} + \frac{\partial w}{\partial z})^{n+1} - (\frac{\partial v}{\partial y} + \frac{\partial w}{\partial z})^n]/\Delta t = (\frac{\partial \psi_2}{\partial y} + \frac{\partial \psi_3}{\partial z})^n - \frac{1}{\rho_0}\nabla^2 p^{*n}. \qquad (32)$$

If the velocity field has no divergence at $t = n + 1$, i.e.:

$$(\frac{\partial v}{\partial y} + \frac{\partial w}{\partial z})^{n+1} = 0 \tag{33}$$

equation (32) becomes:

$$(\frac{\partial v}{\partial y} + \frac{\partial w}{\partial z})^{n}/\Delta t + (\frac{\partial \psi_2}{\partial y} + \frac{\partial \psi_3}{\partial z})^{n} = \frac{1}{\rho_0} \bigtriangledown^2 p^{*n}. \tag{34}$$

Equation (34) is not exactly compatible with the Adams-Bashforth method. Therefore, equation (34) is replaced after DEARDORFF (1973):

$$\frac{2}{3}(\frac{\partial v}{\partial y} + \frac{\partial w}{\partial z})^{n}/\Delta t + (\frac{\partial \psi_2}{\partial y} + \frac{\partial \psi_3}{\partial z})^{n} = \frac{1}{\rho_0} \bigtriangledown p^{*n} \tag{35}$$

4 Results

We made two simulations from initially cloudless, homogenous conditions. The initial mean environment in both experiments had the PBL top at about 1000 m. The inversion above the PBL has a strength of about $2K/100\ m$. The choice of the surface temperature is such that the initial temperature difference between the sea surface and the air is 1 K. Since we are interested in the marine boundary layer in particular, a saturation condition on the humidity is used so that the surface humidity is set equal to the saturated value at the appropriate surface temperature. The geostrophic wind speed is chosen to be $|\vec{v}_g| = 20\ m/s$. The asymptotic mixing length is fixed at 40 m in all runs. These conditions are similar to that observed on September 20 during the 1981 KonTur-experiment where a considerable number of cloud streets were observed (see therefore BRÜMMER, 1985). Values of the main input parameters are given in Table 1.

$z_o = 0.000835\ m$	$f = 1.2 \cdot 10^{-4} s^{-1}$
$z_P = 50\ m$	$\|\vec{v}_g\| = 20\ m/s$
$\lambda = 40\ m$	$\Delta\theta \approx 1\ K$

Tab. 1: Important input parameters

In order to prevent a steady unbounded growth of the boundary layer a large scale subsidence is introduced. The subsidence is set equal to 1.64 cms^{-1} at the top of the model.
In the first experiment the prognostic equations were solved without considering the condensation process. In simulation II we rerun experiment I but with including the condensation process.

4.1 Case I (Dry Case)

4.1.1 Mean Profiles

Vertical profiles for $\tilde{u}$, $\tilde{v}$ *and* $\tilde{\theta}$ ($\tilde{}$ denotes horizontal averaged values) for case I for different times are shown in Fig. 2. Shown are initial profiles (solid), profiles after 1.5 hours (long dashes) and after 2.5 hours (short dashes). The initial temperature profile is characterized by a rather strong gradient in the surface layer and a well mixed layer above. The boundary layer is capped by a strong inversion which is defined by a sharp increase in the temperature gradient above the well mixed layer.

The initial along-roll wind component exhibits a strong wind shear in the surface layer. In the mixed layer the $\tilde{u}$-profile increases with height and reaches an absolut maximum in the upper part of the PBL. The cross-roll wind component is characterized by a tangent like profile.

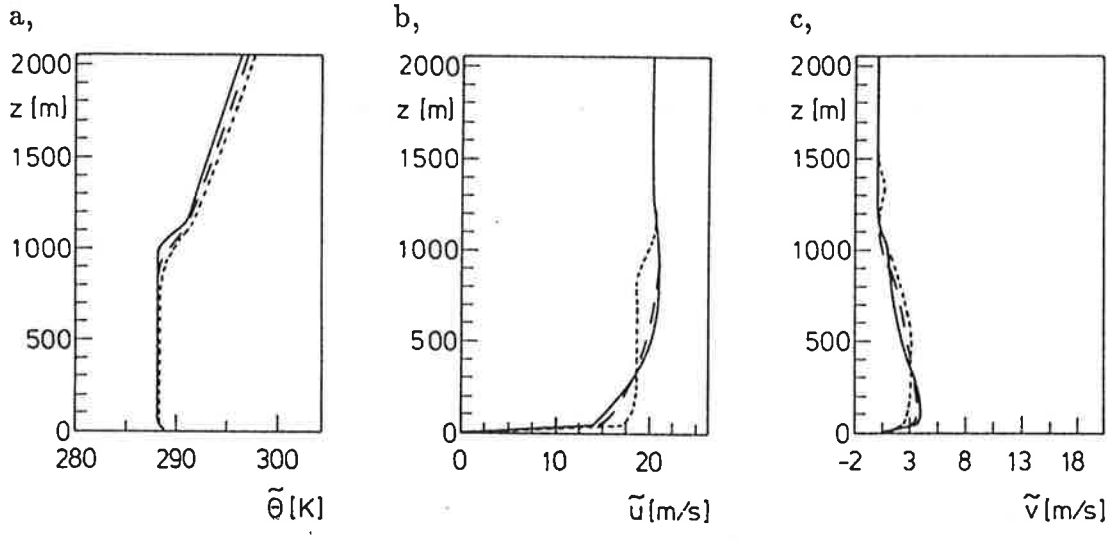

Fig.2a-c: Temporal evolution of the horizontal averaged profiles of $\tilde{\theta}$, $\tilde{u}$ *and* $\tilde{v}$ for case I.

Due to the surface heat flux the mixed layer is warmed and the temperature difference between the sea surface and the air is lowered. Variations of the boundary layer height are (due to the large scale subsidence) small. The mean vertical gradient of the $u-$momentum is (due to the longitudinal momentum transports associated with the rolls) reduced. The $v-$component is enhanced in the most part of the roll layer. Vertical profiles of horizontally averaged variances of the components of the roll motion are presented in Fig. 3. Additionally, the roll-scale vertical transports of longitudinal and lateral momentum and of heat are presented. A comparison between the model statistics and observations is difficult. MASON and SYKES (1982) found that the turbulence statistics have to be averaged over a period of a few hours for an unchanged mean flow to obtain an accurate turbulence statistic. Over this period the mean flow changes significantly in this case. Additionally, one has to keep in mind that the two-dimensionality of the model leads to unrealistic roll-scale variance ratios ($\overline{u'^2}/\overline{v'^2}$) (see CHLOND (1987) and BECKER (1987)). Therefore, one should take the comparison between the measured statistics and the model statistics (which is obtained by averaging results from realizations over a period of twenty minutes starting 1.5 hours after the initial perturbation) not too literally. The measured data are marked with dots and crosses and refer to aircraft measurements from the FALCON and the HERCULES, respectively.

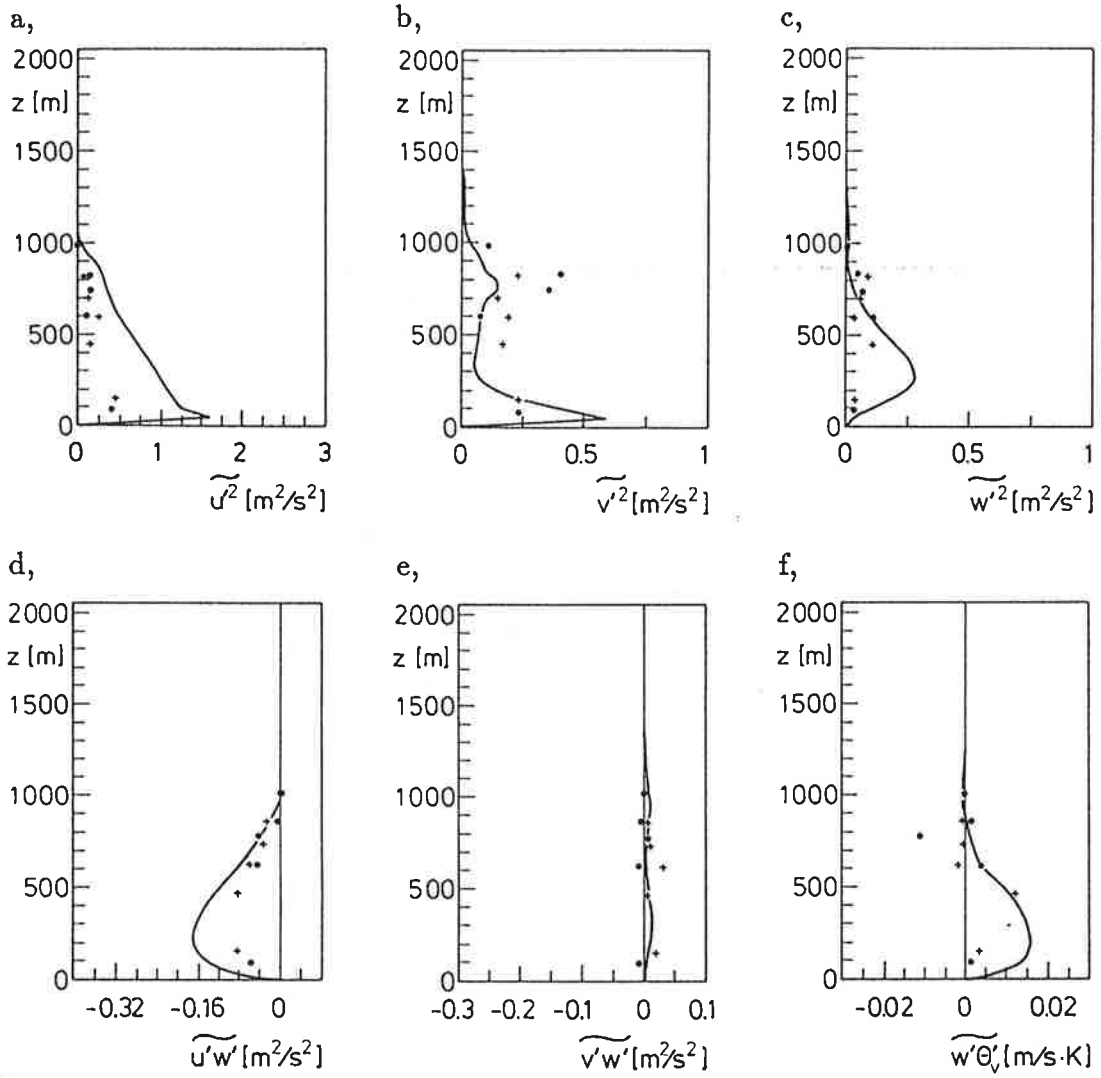

Fig. 3a-f: Vertical profiles of horizontally averaged variances of the longitudinal perturbation velocity, the lateral perturbation velocity and the vertical velocity for case I ($\tilde{u'^2}$, $\tilde{v'^2}$, $\tilde{w'^2}$). Additionally, vertical profiles of the momentum fluxes and the heat flux are shown ($\tilde{u'w'}$, $\tilde{v'w'}$, $\tilde{w'\theta_v'}$). Data are marked with dots and crosses and refer to aircraft measurements from the FALCON and the HERCULES, respectively.

The roll-scale $\tilde{u}'$-variance is large at the surface and decreases with height. The $\tilde{v}'$-variance profile has a quite different shape. The profile has, as expected for a roll circulation, a maximum at the sea surface and a secondary maximum in the upper part of the roll layer. The ratio ($\tilde{u'^2}/\tilde{v'^2}$) is much larger than observed. This is (as mentioned before) a consequence of the two-dimensionality of the model. In a two-dimensional model the longitudinal component is virtually decoupled from the

dynamics of the other component resulting in a storage of energy in this component. The $\tilde{w}'$-variance values increase from the sea surface up to one third of the boundary layer where an absolut maximum of the $\tilde{w}'$-variance occurs. In the upper part of the roll layer the $\tilde{w}'$-variance decreases.
The calculated longitudinal momentum flux profile has a maximum close to the sea surface and decreases rapidly with height to values near zero at the top of the roll layer. The lateral momentum flux is generally smaller than the longitudinal momentum flux. The heat flux profile has high values near the surface and decreases with height. In the upper part of the PBL the downward entrainment of warm air above the inversion leads to a negative vertical heat flux.

4.1.2 Structure of the Secondary Circulation

The roll vortex development starts about 1.5 h after the initial perturbation. Fig. 4a and 4b show realizations of the vertical velocity field for fully developed rolls. Results at time 2 h and 2.08 h are presented. The velocity values shown were normalized using the maximal vertical velocity occuring in the model domain. The first obvious feature of the flow is that they are far from regular. There are some large scale rolls extending to a several hundred meters but there is also some energy in smaller scales. The picture of the flow pattern shown here is in qualitative agreement with model results obtained by MASON and SYKES (1982) and CHLOND (1987).

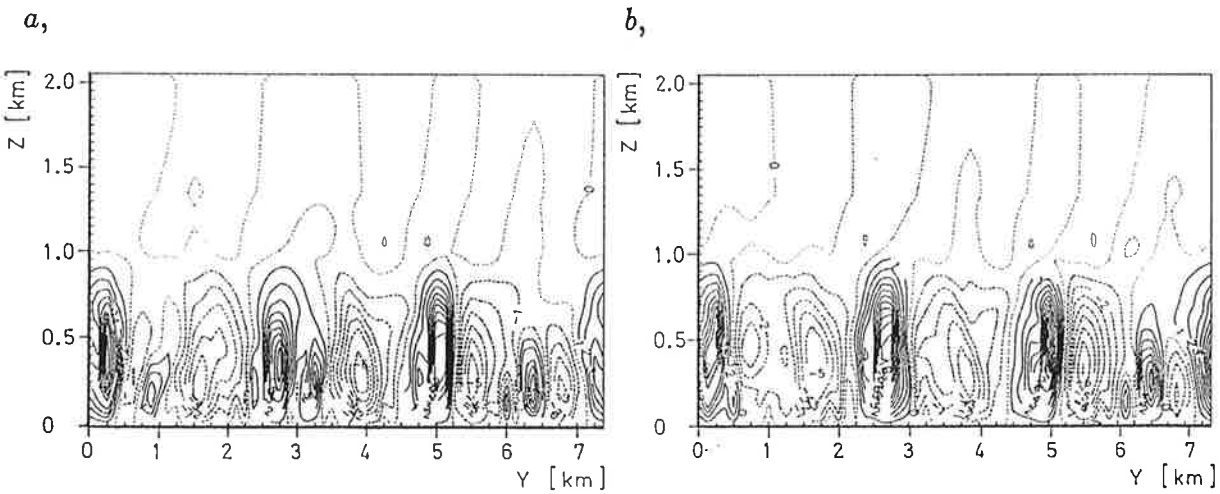

Fig. 4a, b: Realizations of the vertical velocity fields for case I at time $t = 2\ h$ (Fig. 4a) and $t = 2.08\ h$ (Fig. 4b). Solid contours denote positive values, dashed negative values. All values were multiplied by a factor 10.

4.2 Case II (Moist Case)

In our second experiment we rerun the first experiment but with including the condensation process.

4.2.1 Mean Profiles

Vertical profiles for $\tilde{\theta}$, $\tilde{u}$, $\tilde{v}$, $\tilde{q}$ and $\tilde{q_l}$ at time $t = 0\,h$, $t = 1.5\,h$ and $t = 2.5\,h$ are shown in Fig. 5a-e. As mentioned before the initial profiles of wind and temperature are chosen to be the same as in the dry case.

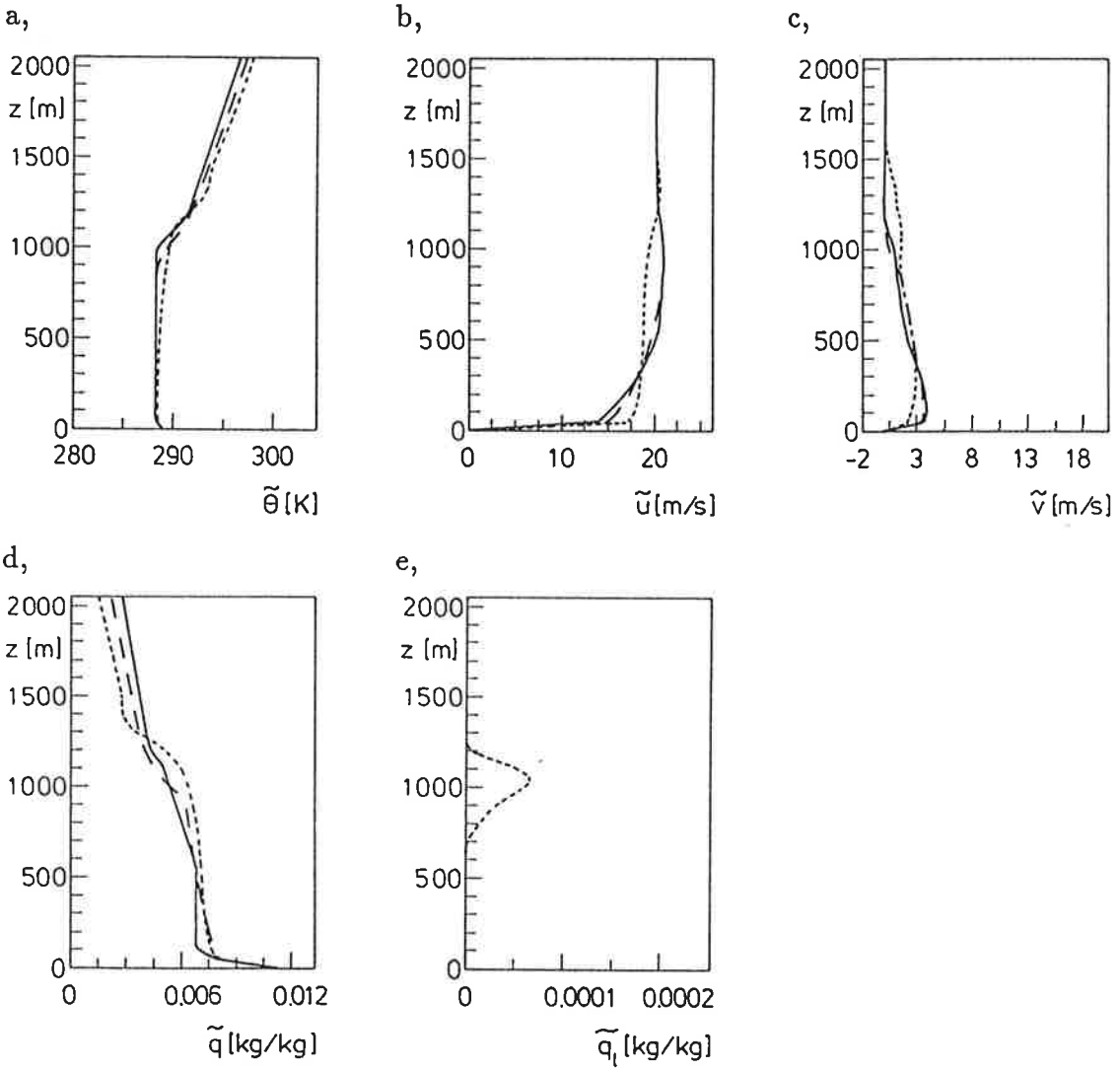

Fig. 5a-e: Temporal evolution of the horizontal averaged vertical profiles of $\tilde{\theta}$, $\tilde{u}$, $\tilde{v}$, $\tilde{q}$ and $\tilde{q_l}$ for case II.

As in the dry case the mixed layer is warmed due to the surface heat flux. The temperature difference between the sea surface and the air is lowered. Beyond that the temperature field is also modified by cloud activity. The cloud layer and the well mixed layer are heated due to latent heat release. In contrast to the dry case a small boundary layer growth is observed which is a result of the latent heat release in the cloud layer. The mean velocity profiles are very similar to that observed in the dry case. Therefore, one can suggest that the direct influence of the cloud field on the wind field is small. The initial specific humidity profile is an almost monotonically-decreasing function of height, except near the surface where the ocean surface yields high humidity values. At all levels in the mixed layer a rise in specific humidity is observed. Vertical profiles of the horizontal averaged liquid water content are shown in Fig. 5e. The liquid water content increases with height in the cloud layer and reaches an absolute maximum in the upper half of the cloud layer. Above this level the liquid water content decreases with height upward to zero at the cloud top. It should be mentioned that the average of the liquid water content of the whole domain shows a large temporal variability with bursts of large liquid water contents seperated by periods with smaller liquid water contents.
Vertical profiles of the velocity variances and the roll-scale transports are presented in Fig. 6. The shown profiles are (as in the dry case) averaged results from realizations over a period of twenty minutes starting 1.5 h after the initial perturbation. As in the absence of clouds the longitudinal velocity variance profile exhibits an absolut maximum near the surface. The values decrease towards the top of the boundary layer. Above 1200 m the longitudinal velocity variance is negligible. The lateral velocity variance has a maximum near the sea surface and a secondary maximum at the top of the roll layer. On the whole the longitudinal and lateral velocity variance profiles are very similar to that in the dry case. The relation $(\tilde{u'^2}/\tilde{v'^2})$ is nearly the same as in the dry case. The $\tilde{w}'$-variance profile increases with height and reaches an absolut maximum in the first third of the roll layer. In the upper part of the roll layer the $\tilde{w}'$-variance values decrease. In the cloud layer the latent heat release leads to $\tilde{w}'$-variance values which are somewhat larger than in the dry case. The profiles of the longitudinal and the lateral momentum flux are very similar to those in the absence of clouds. The largest effect of the condensation process is seen in the heat flux. In the moist case the heat flux profile exhibits beyond the local maximum near the sea surface a second local maximum in the cloud layer. Due to the weak cloud activity in this case the second maximum of the heat flux profile is of course not very strong. In the upper part of the cloud layer the heat flux decreases slowly to slightly negative values at the inversion. The humidity flux increases up to a height 350 m below the cloud base. Above this level the moisture flux decreases with height upward to zero at the cloud top.

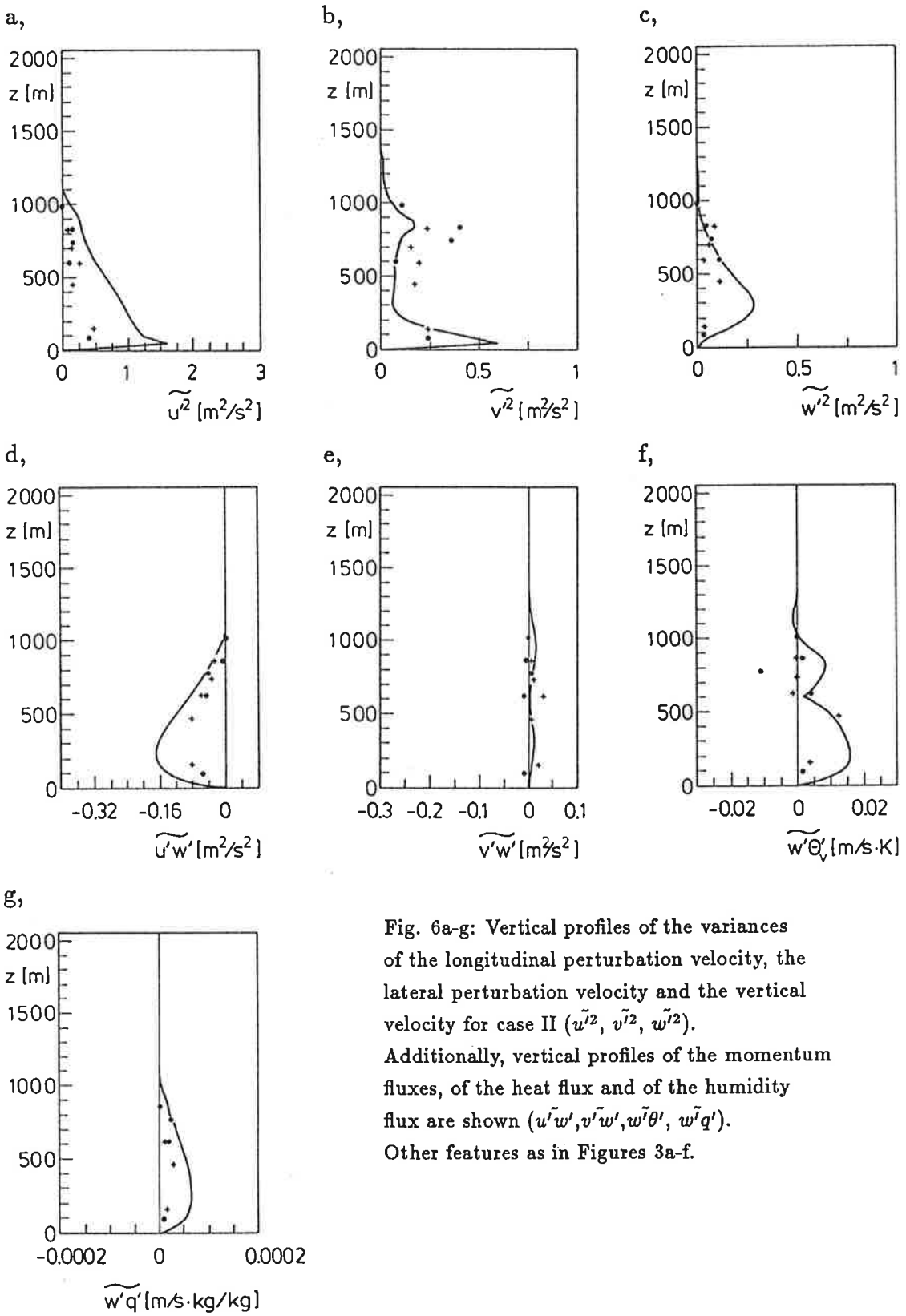

Fig. 6a-g: Vertical profiles of the variances of the longitudinal perturbation velocity, the lateral perturbation velocity and the vertical velocity for case II ($\tilde{u'^2}$, $\tilde{v'^2}$, $\tilde{w'^2}$). Additionally, vertical profiles of the momentum fluxes, of the heat flux and of the humidity flux are shown ($\tilde{u'w'}$,$\tilde{v'w'}$,$\tilde{w'\theta'}$, $\tilde{w'q'}$). Other features as in Figures 3a-f.

4.2.2 Structure of the Secondary Circulation

As in the dry case the roll vortex development starts 1.5 h after the initial perturbation. Fig. 7a-d show typical realizations of the vertical velocity fields and the corresponding liquid water fields for fully developed rolls. The velocity and liquid water values were normalized using the maxima of these quantities occuring in the domain. Results at time 2 h and 2.08 h are presented. The flow structure appears similar to that found in a dry inversion-capped convective boundary layer case. The flow is again dominated by boundary layer rolls which are not steady in form or highly regular. Four counterrotating vortex pairs are to be seen. The maximum vertical velocity reaches more than 1.5 m/sec.
Clouds, the word cloud referring to regions where q_l is positive occur between 700 and 1000 m. The maximum liquid water content reaches $.1g/kg$ (Fig. 7c) and $.12g/kg$ (Fig. 7d) which seems to be reasonable for small cumuli. Cloud cover varies between 30% and 40%. A strong positive correlation between the two fields of liquid water and the vertical velocity is clearly apparent. This strong correlation was also observed by MASON (1985) who investigated a similar case of roll motion. The clouds are characterized by ascending motions surrounded by regions with descending motions. A truncation error (which leads to small negative liquid water contents) is sometimes noticable around cloud base. This deficiency seems to be common for the condensation formulation used in this study (see therefore also SOMMERIA, 1976) and could be corrected by using a better resolution. Better results might also be possible by using the concept of the liquid water potential temperature. However, the occuring negative liquid water contents are very small in this study. Therefore, the chosen procedure seems to be justified.
The inversion observed at the top of the cloud layers acts as a "lid" to further vertical development and, thus the rise of cumulus clouds is hindered.
In order to compare the predicted aspect ratio with the observations the horizontal distance of the neighbouring updrafts was determined every time step during an averaging period. The time interval was chosen in a way that the KonTur conditions were roughly fulfilled during the averaging period. The time averaging interval was a period of twenty minutes starting 1.5 h after the initial perturbation. The average aspect ratio was determined to be about three which is consistent with observations by BRÜMMER, 1985. It should be mentioned that four hours after the initial perturbation (the KonTur conditions are no longer fulfilled) a roll spacing was observed. However, the model does not treat motions of a scale larger than 7 km. Therefore, a larger model version should be used before any general conclusion on this topic can be made.

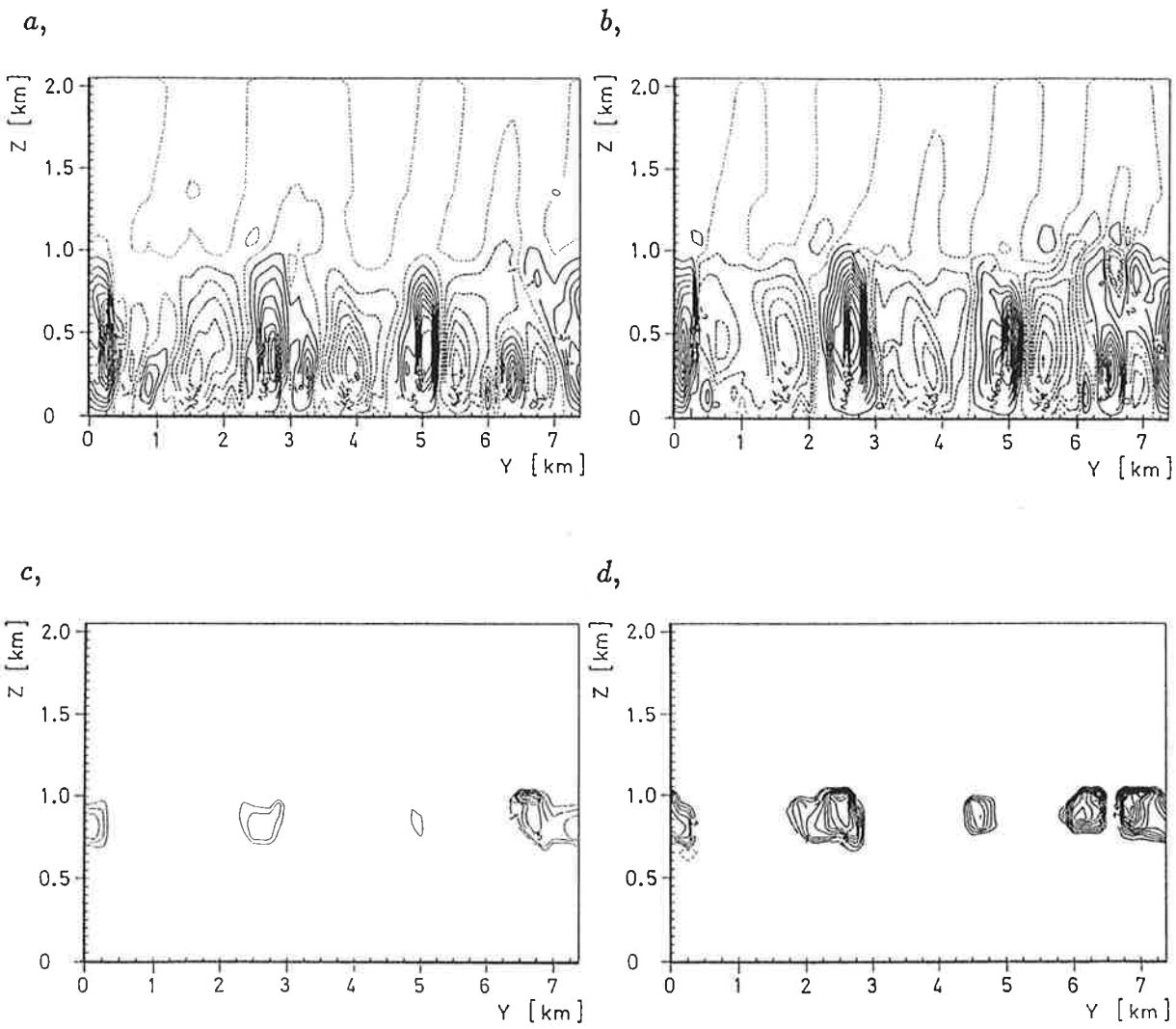

Fig. 7a-d: Realizations of the vertical velocity field and the corresponding liquid water field for case II at time $t = 2\ h$ (Fig. 7a and 7c) and $t = 2.08\ h$ (Fig. 7b and 7d). Solid contours denote positive values, dotted negative values. The velocity and liquid water values were normalized by using the maxima of these quantities occuring in the domain. All values were multiplied by factor 10.

4.3 Conclusions

In this paper we have presented the results on boundary layer rolls from a study of a two-dimensional grid point model which contains a water cycle with cloud formation. Our interest was to examine the influence of the clouds on the secondary circulation,

and the model statistics.
In the dry case the flow field showed a pattern with a typical helical roll secondary circulation. The flow pattern as well as the model statistics were similar to that obtained by MASON and SYKES (1982) and CHLOND (1987).
In the presence of moisture, the flow field showed again a pattern with a roll circulation which was similar to that obtained in the dry case. Clouds occurred at the top of the updraughts of the boundary layer rolls (if the boundary layer was sufficient humid).
The secondary flow statistics as well as the geometrical roll parameters and the cloud generation were compared with observations. The predicted roll parameters (which were very similar for the dry and the moist case) and the cloud generation were in the limits to be observed. The secondary flow statistics could (in the dry and in the moist case) only be qualitatively reproduced by the model. The largest effect of condensation is seen in the heat flux. In the moist case the heat flux showed beyond the local maximum near the surface layer a secondary maximum in the cloud layer which led to slightly larger vertical velocity variances in the cloud layer than in the dry case. The influence of the latent heat release on the wind field seems to be on the whole not crucially important. However, one has to keep in mind that all results are very sensitive to liquid water content and therefore sensitive to the large scale parameters (especially large scale subsidence) which are often rather unknown parameters. More parameter combinations of air-sea temperature difference, mean wind speed and large scale parameters should be used before further general statements can be made.

Acknowledgement

The author wish to thank Prof. Dr. H. Hinzpeter, Prof. Dr. B. Brümmer and Dr. A. Chlond for many helpful discussions and comments. Thanks also to M. Grunert and M. Lüdicke for preparing the figures.

5 Nomenclature

variable	meaning
c_P	specific heat coefficient at constant pressure
f	Coriolis parameter
g	gravitational acceleration
$k_m, k_\theta, k_q, k_{q_l}$	subgrid eddy coefficient for momentum, heat, humidity and liquid water content
l	mixing length
L_v	specific latent heat for vaporization
p	pressure
q	specific humidity
q_l	specific liquid water content
q_s	saturation specific humidity
Ri	Richardson number
x, y, z	coordinate axes
u, v, w	velocity components in respective x, y, z directives
u_g, v_g	components of the geostrophic wind
u_*	"friction" velocity
z_0	roughness length
z_P	height of the surface layer
Δt	time step increment
$0(subscript)$	a constant reference value

$S(subscript)$	a synoptic value
ϵ	ratio of molecular masses for water vapour and air
θ	potential temperature
θ_v	virtual potential temperature
θ_{vl}	potential temperature taking into account the weight of liquid water
θ_*	temperature scale
λ	asymptotic mixing length
κ	von Kármán constant
Φ_M, Φ_H	universal stability functions
ρ	density

6 Literature

BECKER, P., 1987: Three-dimensional investigations of roll-vortices: a case study. Beitr. Phys. Atmosph. 60, 170-179.

BLACKADAR, A.K., 1962: The vertical distribution of wind and turbulent exchange in a neutral atmosphere. J. Geophys. Res. 67, 3095-3102.

BROWN, R.A., 1970: A secondary flow model for the planetary boundar layer. J. Atmos. Sci. 27, 742-757.

BRÜMMER, B., 1985: Structure, dynamics and energetics of boundary layer rolls from KonTur aircraft observations. Beitr. Phys. Atmosph. 58, 237-254.

BUSINGER, J.A., J.C. WYNGAARD, Y. IZUMI and E.F. BRADLEY, 1971: Flux relationships in the atmospheric surface layer. J. Atmos. Sci., 28, 181-189.

CHLOND, A., 1987: A numerical study of horizontal roll vortices in neutral and unstable atmospheric boundary layers. Beitr. Phys. Atmosph. 60, 144-169.

DEARDORFF, J.W., 1973: The use of subgrid transport equations in a three-dimensional model of atmospheric turbulence. J. Fluids Eng. 95, 429-438.

DEARDORFF, J.W., 1973: Three-dimensional numerical modelling of the planetary boundary layer, Workshop on Micrometeorologie, Duane A. Haugen, Ed. Amer. Meteor. Soc. 271-311.

DUTTON, J.A. and G.H. FICHTEL, 1969: Approximate equations of motion for gases and liquids. J. Atmos. Sci. 26, 241-254.

KUETTNER, J.P., 1971: Cloud bands in the earth's atmosphere. Tellus 23, 404-425.

LE MONE, M.A., 1973: The structure and dynamics of horizontal roll vortices in the planetary boundary layer. J. Atmos. Sci. 30, 1077-1091.

MASON, P.J. and R.I. SYKES, 1980: A two dimensional numerical study of horizontal roll vortices in a neutral atmospheric boundary layer. Quart. J. R. Meteorol. Soc. 106, 351-366.

MASON, P.J. and R.I. SYKES, 1982: A two-dimensional numerical study of horizontal roll vortices in an inversion capped planetary boundary layer. Quart. J. R. Meteorol. Soc. 108, 801-823.

MASON, P.J., 1985: A numerical study of cloud streets in the planetary boundary layer. Bound. Layer Meteorol. 32, 281-304.

SOMMERIA, G., 1976: Three-dimensional simulation of turbulent processes in an undisturbed trade wind boundary layer. J. Atmos. Sci. 33, 216-241.

SYKES, R.I., LEWELLEN, W.S. and D.S. HENN, 1988: A numerical study of the development of cloud-street spacing. J. Atmos. Sci. 18, 2557-2569.

WIPPERMANN, F.K., D. ETLING and H.J. KIRSTEIN, 1978: On the instability of a PBL with Rossby number similarity. Part 2. Bound. Layer Meteorol. 15, 301-321.